

# An Atomic Perspective of a Doped Metal-Oxide Interface<sup>†,‡</sup>

E. A. A. Jarvis and E. A. Carter\*

Department of Chemistry and Biochemistry, University of California, Los Angeles, Box 951569, Los Angeles, California 90095-1569

Received: March 6, 2002; In Final Form: May 3, 2002

We employ density functional calculations to present a detailed picture of the atomic-level interactions at doped  $\text{Al}_2\text{O}_3/\text{Ni}$  interfaces. In particular, we emphasize the importance of local structural and electronic relaxation in determining the global adhesion between metal/ceramic couples. We find localized metal–metal and dopant metal–oxo bonding can produce strong interface adhesion even where no new interfacial reaction product is formed, driven by a combination of oxide donation to dopant acceptor orbitals along with localized covalent dopant metal–oxo and several types of metal–metal bonds. Understanding the local mechanisms of strengthening heterogeneous interfaces may result in practical advances ranging from coating to catalytic applications.

## Introduction

In current solid-state technology, many of the most interesting scientific problems relate to understanding structures such as surfaces, thin films, and interfaces. The practical importance of such structures assumes a variety of guises; in particular, advancing catalysis and coatings design is of scientific, environmental, financial, and engineering interest. Predictive optimization of materials for these applications requires understanding relevant gas–surface as well as solid-state heterogeneous interface interactions.

The past two decades marked an explosion of experimental and theoretical advances in treating gas–surface interactions. In particular, detailed experimental characterization of small molecules interacting with crystalline metal substrates has provided an absolute standard for simulations, allowing significant advances in rigorous theoretical treatment and understanding of these systems.<sup>1,2</sup> It has been shown that often a detailed description, one that recognizes geometric and electronic complexities, of a molecular adsorbate is required to accurately describe its sticking probability on even a simple, single-crystal metallic surface.<sup>3,4</sup> Of course, for chemisorbed gas–surface systems, requirements for an accurate, high-level theoretical treatment are even more severe.<sup>5</sup>

Although experimental advances now allow fairly in-depth characterization of many adsorbate–surface systems, a comparable level of detailed experimental characterization at heterogeneous interfaces generally remains elusive. Reasons for this discrepancy are clear when one considers the experimental limitations distinguishing the two cases. In characterizing gas–surface interactions, the primary crucial aspects are achieving highly controlled experimental conditions and nondestructive, high-resolution means of characterization. In interface studies, even if these objectives are attained, an inherent difficulty remains. An interface is, by definition, mostly internal, thus limiting a detailed characterization of local geometric and electronic states. Furthermore, the large-scale 2D nature of an

interface generally necessitates inclusion of defects, which places limitations on the reproducibility of interface studies. Of course, the fact that many heterogeneous interfaces are at least mildly reactive adds an additional “layer” of complexity in both the literal and figurative sense. Accordingly, providing a detailed picture of interface interactions remains a challenge, even with state-of-the-art experimental techniques.

Simulations must confront a different set of challenges regarding interface characterization.<sup>6–8</sup> These relate to the potentially vast disparity in relevant length and time scales that must be included for an accurate description of the physical system.<sup>9</sup> Work is in progress to couple length scales such that a system size of physical interest might be treated without requiring highly restrictive assumptions regarding the types of interactions that are permitted to take place.<sup>10,11</sup> Electronic structure methods that scale linearly with system size may eventually overcome much of the length scale dilemma.<sup>12,13</sup> For insulators, the localization of electron density can be exploited to result in computationally efficient treatment of large systems.<sup>14,15</sup> Although localization techniques generally are not applicable to metallic systems,<sup>16</sup> the valence electron density of a simple metallic system might be adequately expanded in a fairly small basis, also leading to improved computational efficiency and allowable system size. Furthermore, linear scaling methods that do not rely on orbital localization schemes are especially useful in this case.<sup>12</sup> Nevertheless, at this time, most simulations must either severely limit the size of the system or the number of variational degrees of freedom permitted in the calculation via limited self-consistency, constrained ionic relaxations, etc.

We previously reported the importance of local bonding at heterogeneous interfaces.<sup>17,18</sup> In those works, we highlighted the large increase in adhesion strength at  $\text{Al}_2\text{O}_3/\text{Ni}$  interfaces doped with early transition metals compared to the much weaker clean interface or an interface “doped” with Ni, Al, or Si. That local bonding should play a dominant role in interface stabilization is contrary to previous theories that have assumed electrostatic (image charge) and van der Waals effects dominate adhesion in nonreactive couples.<sup>19–21</sup> The simulations supporting these theories to the exclusion of local bonding effects did suffer

<sup>†</sup> Part of the special issue “John C. Tully Festschrift”.

<sup>‡</sup> We are pleased to honor John Tully, a true giant in the field of surface science theory, with our contribution.

\* Corresponding author. E-mail: eac@chem.ucla.edu.

from a limited inclusion of self-consistency/degrees of freedom mentioned above. Here, we focus on the importance of local bonding to the interface adhesion of  $\text{Al}_2\text{O}_3/\text{Ni}$  and rationalize, based on electronic structure analysis of more variationally complete electronic wave functions, how some elements can be particularly effective in creating strong interface adhesion.

We investigate the interface formed between a nickel substrate and a thin alumina overlayer and characterize the local effects of chemically doping this interface.  $\text{Al}_2\text{O}_3/\text{Ni}$  has practical importance for such uses as protective coatings on jet engine turbines and supported metal catalysts.<sup>8,22</sup> For instance, a  $\text{Ni}/\text{Al}_2\text{O}_3$  catalyst has been suggested for use in alternative energy sources such as fuel cells, since it is a well-known reforming catalyst,<sup>23–25</sup> and more recently in nanotechnology applications, where it has been used to grow carbon nanotubes.<sup>26</sup> In turbine coating technology, it is observed that certain dopants extend the lifetime of the ceramic coating's adherence to the underlying metal alloy. The mechanisms responsible for this improvement remain unclear. Chemical bonding has been suggested as a possible means by which these dopants improve coating lifetimes.<sup>27</sup> However, most recent discussions of the roles of the dopants in coating lifetime improvements do not concentrate on this bonding mechanism, instead focusing on sulfur gettering,<sup>28,29</sup> limiting oxidation of the underlying metal alloy,<sup>30</sup> etc. It is likely that different dopants function with varied mechanisms to help limit de-adhesion, and there is still much to be learned before optimal coatings can be achieved.<sup>17,31,32</sup>

Despite the complicated alloy composition of turbine coatings and the harsh operating environment of engine operation, the metal/ceramic interface formed in thermal barrier coatings is relatively simple. For metal alloys containing a sufficient fraction of Al, a sharp interface of (mostly Ni) alloy with  $\alpha\text{-Al}_2\text{O}_3$  forms as a result of high-temperature oxidation.<sup>33,34</sup> Accordingly, although we are limited in allowable system size, the interfaces modeled here are likely to be physically relevant to approximate the Ni alloy/oxidation product of typical thermal barrier coatings with dopant segregation to the interface, as well as perhaps the  $\text{Ni}/\text{Al}_2\text{O}_3$  interface present in reforming catalysts at elevated temperatures.

## Theoretical Methods

Our calculations are performed in both spin-polarized and non-spin-polarized implementations of density functional (DFT)<sup>35</sup> calculations using the Vienna Ab Initio Simulation Package (VASP).<sup>36</sup> The use of periodic boundary conditions permits simulation of "infinite" interfaces inasmuch as there are no edge effects. Naturally, computational limitations do limit system size such that long-range relaxations are not included. The valence electron density is expanded in a plane-wave basis, and the nuclei and core electrons are replaced with ultrasoft pseudopotentials.<sup>37</sup> For additional transferability and accuracy, non-linear partial core corrections to exchange and correlation are included for all of the metal atoms. Although we performed some test calculations within the local density approximation (LDA) to the exchange-correlation potential, the detailed analysis reported here is obtained from calculations using the generalized gradient approximation (GGA) of Perdew and Wang (PW91).<sup>38</sup> Dipole corrections perpendicular to the interface were calculated but did not significantly alter the energetics.

The ultrasoft pseudopotentials employed in this study are those supplied in the database of VASP version 4.4. These pseudopotentials, generated using the RKKJ scheme,<sup>39</sup> are of the separable Kleinman–Bylander form.<sup>40</sup> The local component of the pseudopotential is the all-electron potential that has been

unscreened with respect to the valence electrons beyond a given radius and smoothly matched at this radius to a zeroth-order Bessel function for the oxygen and transition metal pseudopotentials employed in this study. In the case of Al and Si, the local component corresponds to the d pseudopotential. The database contains similar sets for both the LSDA of Perdew–Zunger<sup>41</sup> and the GGA (PW91)<sup>38</sup> parameterization of the exchange-correlation functional. The employed pseudopotentials were generated in the neutral  $4s^13d^9$ ,  $3s^23p^1$ ,  $2s^22p^4$ , and  $3s^23p^2$  configurations for Ni, Al, O, and Si, respectively. The early transition metal pseudopotentials (Sc, Ti, Y, and Zr) were generated within the neutral  $s^1$  configuration, and each allows self-consistent treatment of the semi-core p states as well as the valence s and d.

The calculations consisted of four steps: bulk  $\text{Al}_2\text{O}_3$  and nickel calculations,  $\text{Al}_2\text{O}_3(0001)$  and  $\text{Ni}(111)$  surface calculations,  $\text{Ni}(111)\text{-X}$  and  $\text{X-Al}_2\text{O}_3(0001)$  doped surface calculations (with dopant "X"), and  $\text{Al}_2\text{O}_3(0001)/\text{X}/\text{Ni}(111)$  doped interface calculations. For the bulk calculations, we tested for convergence of the  $\mathbf{k}$ -point sampling density and kinetic energy cutoff and relaxed the atomic and cell coordinates. For the surface calculations, we also converged the surface energies with respect to slab and vacuum thickness and atomic relaxations. We initially relaxed the surface and interface structures with a 40% lower kinetic energy cutoff for the plane-wave basis. Once we obtained the optimized ionic coordinates with this smaller basis, we further relaxed the ionic coordinates with the converged plane-wave basis. This allowed faster convergence of the structures, and several test cases showed this did not affect the final geometries.

In our calculations, we imposed the constraint of having stoichiometric alumina slabs with equivalent faces of a 1/3 monolayer Al termination. This termination generally appears to best approximate the UHV ( $1\times 1$ ) termination of the (0001) surface.<sup>42–45</sup> The  $\text{Ni}(111)$  surface presents a unique cleavage plane with half of the 3-fold hollow sites classified as hcp and the other half as fcc. The larger metallic radii of these early transition metals would result in large compressive strains if a full monolayer of epitaxial coverage was formed on the  $\text{Ni}(111)$  surface. Instead, a half-monolayer of dopant atoms were deposited, positioned to initially cover half of the fcc hollow sites. Then they were relaxed, using a conjugate gradient algorithm, to more favorable coordinates over the course of the simulation. We chose to impose the equilibrium bulk Ni lattice constants on our interface unit cells, since we are modeling a thick, doped nickel substrate with a thin alumina coating. In the ionic relaxation steps, the coordinates of the nickel atoms in the bottom layer of the nickel slab were fixed to bulk values to ensure bulk-like nickel away from the interface. This aided in computational efficiency, and a few test cases indicated these restrictions had little to no effect on the interface itself.

The interface lattice mismatch between the  $\text{Ni}(111)$  and  $\text{Al}_2\text{O}_3(0001)$  in our calculations was only 3% for a hexagonal cell with a surface area of  $21.4\text{ \AA}^2$ . Hence, the results obtained with imposed Ni lattice vectors were similar to several test cases using alumina lattice vectors. To further test whether our relaxed structures were perhaps trapped in unfavorable local minima, a few relaxed structures were annealed, using Nosé's algorithm for constant temperature DFT-MD<sup>46</sup> at 1200 K using a time step of 0.40 fs for a few tenths of a picosecond. The annealed structures were then quenched using the conjugate-gradient algorithm also employed in the relaxations of the initial structures previously described. These annealing runs resulted in similar structures and did not indicate a strong preference

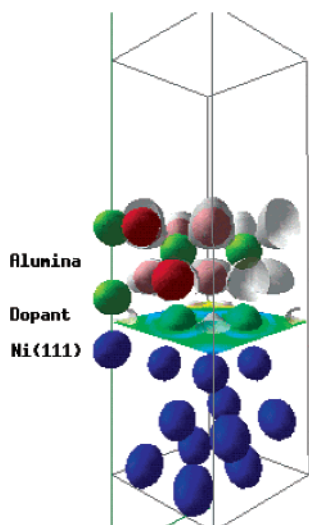


**Figure 1.** Periodic supercell with the  $\text{Al}_2\text{O}_3(0001)/\text{dopant}/\text{Ni}(111)$  interface structure.

toward interface reactivity to produce a new oxide with the dopant. Accordingly, we limit our discussion in the results to the non-annealed structures. Of course, we cannot rule out the possibility that with significantly longer annealing times and/or higher temperature, additional features might have been observed.

A picture of the periodic interface supercell is shown in Figure 1 with the Ni(111) substrate, representative dopant ions at the interface, and the  $\text{Al}_2\text{O}_3$  coating. The Ni substrate was three monolayers (ML) thick; we found this thickness to effectively simulate a thick slab by producing similar surface energies and relaxations as thicker slabs. The two ML alumina coating is the thinnest stoichiometric  $\text{Al}_2\text{O}_3$  coating that can maintain planar hexagonal arrays of oxygen ions as in the corundum structure. This thickness also corresponds to relevant thicknesses for epitaxial alumina growth on  $\text{Ni}_3\text{Al}$ .<sup>47–50</sup> In thermal barrier coating applications, although the alumina does provide a slow-growing protective oxide, it is much thicker, i.e., roughly several micrometers thick.<sup>51</sup>

Providing a means for setting the partial band occupancies for the metal is needed to obtain accurate descriptions of the total energy. We employed both the tetrahedron method with corrections introduced by Blöchl et al.<sup>52</sup> and first-order Methfessel–Paxton smearing.<sup>53</sup> For these calculations, we chose a smearing width of 0.1 eV, which resulted in very small entropy terms (less than 0.5 meV/atom). Both methods gave the same total energies to within less than 0.5 meV/atom for our calculations. The analysis in the results section is based on partial occupancies obtained with the smearing method.

For analysis of local charge densities, local density of states (LDOS), projection spheres around each atom must be defined. We defined spheres with radii of 1.015 Å and 1.345 Å for the Al and O, respectively, in the alumina coating and 1.23 Å for Ni ions in the Ni(111) substrate. The radii for the dopant ions were chosen to be 1.10 Å for Si and Al, 1.23 Å for Ni, and 1.50 Å for the early transition metal dopants. These spheres have no impact on the total energy or density convergence in the calculation but merely determine the amount of charge density enclosed within the predetermined sphere around each atom for post-DFT-calculation analysis purposes. The Al and O radii were chosen to capture most of the cell volume of bulk alumina with minimal overlap; these radii describe a crystal of ~80% ionic character for the “bulk structure” expanded by 3% to fit the nickel substrate. Estimates ranging from ~60% to

~90% ionic character have been reported previously.<sup>54–57</sup> The sphere radii for Al and O were able to capture most of the electron density; however, the Ni radius resulted in ~1.25  $e^-$  per atom in the interstitial regions due to the delocalized valence density of the metal. Similarly, the radii for the early transition metals only captured ~80–90% of the total electron density for the neutral metal in the bulk and in the interface environment. These radii for the metals were maintained to minimize sphere overlap in our analysis of charge differences between atoms in the isolated slabs and the interfacial structures. A more complete description of the effects of projection radii choices is provided in the next section.

## Results and Discussion

Previously, we have discussed the interesting trends in adhesion at the ideal  $\text{Al}_2\text{O}_3/\text{Ni}$  interface with increasing alumina coating thickness.<sup>22</sup> Likewise, we showed that introducing dopants at this interface could dramatically alter the calculated adhesion.<sup>17,18</sup> In particular, the calculated adhesion increases dramatically with early transition metal doping. In fact, Ti is able to effectively double the adhesion relative to Ni; and Sc, Zr, and Y all increase the calculated adhesion by 70–80% relative to Ni. Conversely, compared to Ni, Al or Si additions decrease the doped metal–ceramic adhesion by ~20–30%. As mentioned, we attribute the dramatic increase in adhesion for the early transition metal dopants to local bonding interactions at the interface.<sup>18</sup> Here, we provide a detailed picture of those interactions.

The individual bonds involved in localized interactions at the interface should fit primarily into one of three categories: ionic, covalent, and/or donor–acceptor. Metallic bonding can also contribute “delocalized” bonding at the interface. Finding means by which to distinguish and quantify these bonding interactions is not always straightforward. In this section, we use several methods to analyze the bonding that occurs as a result of interface formation. These include LDOS and integrated LDOS analysis to investigate the available electronic states on each type of atom and the occupancy of those states, as well as density difference plots to explore the modifications of the electron density with interface formation.

Ionic interactions at complicated interface structures present several possible signatures. Perhaps the most straightforward of these can be evident through a simple comparison of density differences between the interface and the sum of the isolated coating and substrate. Similarly, ionic bonding may appear as depletion of occupied valence states (decreased valence band LDOS) on the cation concurrent with increased occupied states on the anion. This means of characterizing ionic bonding is subject to the caveats discussed later regarding choice of LDOS projection sphere sizes and generally cannot be considered reliable unless a concurrent loss–gain relationship is observed, since, for example, delocalized metallic states also may result in decreased local occupancy. Another possible signature of ionic bonding is a possible shift in core eigenvalues (although the change in Madelung potential can work to counteract this shift).<sup>58</sup>

Covalent bonding may be seen in the electronic structure as mixing of the LDOS between two species to form bonding and antibonding states. Likewise, covalent bonding can be seen as a buildup of electron density between two nuclei. Analysis of the electron localization function (ELF)<sup>59</sup> values can provide a measure of the degree of covalent bonding between species as well, but is a somewhat unsatisfying measure for non-norm-conserving representations of the kinetic energy density. Polar



**TABLE 1: Local Bond Lengths and Coordination Numbers around the Unique Dopant Ion Sites at the 0.5 ML-doped Al<sub>2</sub>O<sub>3</sub>/Ni Interface<sup>a</sup>**

	interface dopant "X"						
	Ni	Al	Si	Sc	Y	Ti	Zr
"X"-O bond length	1.97 1.95	1.69 1.69	1.67 1.66	2.51 2.51	2.55, 2.61 2.52, 2.60	2.12, 2.15, 2.29 2.13, 2.15, 2.30	2.52 2.54
"X"-O coordination	1	1	1	3	~2	~2-3	3
"X"-Ni bond length	2.39 2.38	2.21, 2.46, 2.47 2.29, 2.29, 2.65	2.12, 2.44, 2.45 2.17, 2.22, 2.51	2.57 2.57	2.75 2.76	2.26, 2.59 2.25, 2.65	2.66 2.65
"X"-Ni coordination	3	~1-3	~1-3	3	3	~1-2	3
"X"-Al distance	2.54 2.60	2.63 2.75	2.58 2.66	3.09 3.09	3.10 3.10	2.81, 2.85, 2.97 2.81, 2.84, 2.98	3.07 3.08
"X"-Al coordination	~1	~1-2	~1	~3-4	~3	~2-3	~3-4
"X"-X distance	2.44, 2.54 2.44, 2.54	2.87 2.87	2.53, 2.78 2.53, 2.78	2.87 2.87	2.87 2.87	2.68, 2.98 2.68, 2.98	2.87 2.87
"X"-X coordination	~2	3	~2	3	3	~1-3	3
Ni-Al bond length	3.06	2.19, 2.54, 2.57	2.25, 2.42, 2.46	2.25	2.28	2.26	2.27
calculated adhesion (mJ/m <sup>2</sup> )	1880	1490	1240	3350	3240	3690	3210

<sup>a</sup> The shortest Ni-Al bond distance between Ni(111) and Al<sub>2</sub>O<sub>3</sub>(0001) at each interface is also included. For point of reference, the calculated adhesion<sup>17,18</sup> at the Al<sub>2</sub>O<sub>3</sub>/X-Ni interface is also provided.

covalent bonding may be less readily apparent from a plane-wave representation of the pseudo-electron density. As with true covalent bonding, density plots for polar covalent bonding should display an electron density buildup between the nuclei; but in the polar covalent case, this density will be primarily associated with the more electronegative ion. Accordingly, integrated LDOS will display a significantly greater electron density gain on the more electronegative species. Of course, in the limit of highly polar covalent bonding, the interactions will approach the signatures for ionic bonding.

The appearance of donor-acceptor bonding also may be subtle from the standpoint of available means by which to quantify this effect. It could be that the most obvious modification of the electronic states appears in the unoccupied states on the acceptor atom. These empty states on the acceptor will be partially occupied as a result of the donor-acceptor bonding; hence, a decrease in the states above the Fermi level upon bond formation is anticipated with this type of bonding. Density difference plots might not display dramatic features for donor-acceptor bonding since it is likely that a localized, lone-pair density was present in that spatial region prior to the donor-acceptor bond formation. Nevertheless, as with covalent bonding, an electron density increase in the region between the nuclei is likely to be evident if donor-acceptor bonding exists.

As a starting point for discussing the specific bonds that are formed at these doped interfaces, it is necessary to have a sense of the local geometry around the dopant atoms of interest in this study. Table 1 shows the bond lengths and coordination numbers of the unique interfacial atomic sites involved in local bonding at the periodic interface structure. The calculated adhesion at the Al<sub>2</sub>O<sub>3</sub>/X-Ni interface site is also included for purposes of comparison. We find a strong correlation between coordination number and adhesion strength. In particular, the early transition metals all exhibit higher dopant-O coordination (i.e., ~2-3 relative to singly coordinated Ni, Al, and Si), correlating with the dramatic increase in adhesion for these interface dopants.

A comparison of these dopant-oxo bond lengths to those in the respective perfect crystal oxides gives a sense of how the bonding at this interface is expected to differ from the bulk oxides. The "dopant" Al-O bond is 9% shorter than the shortest (1.86 Å) Al-O bonds in Al<sub>2</sub>O<sub>3</sub>. Similarly, the "dopant" Ni-O bond is shorter than in NiO crystal (2.08 Å), but only by ~6%.

All other dopant-O bonds are longer than the respective bonds in representative oxide crystal structures for those elements, with Si-O ~3% larger than in  $\alpha$ -quartz (1.61 Å), Ti-O ~9-17% larger (for the shortest-longest interface Ti-O bonds) than in rutile TiO<sub>2</sub> (1.95 and 1.98 Å), Zr-O 15% longer than in cubic ZrO<sub>2</sub> (2.20 Å), and Sc-O and Y-O roughly 10-15% longer than the bixbyite oxide bond lengths (~2.2-2.3 Å for Y<sub>2</sub>O<sub>3</sub>).<sup>60</sup> The significantly longer X-O bond lengths of the early transition metals indicate that the X-O bonding character is likely to be very different at the doped Al<sub>2</sub>O<sub>3</sub>/Ni interface compared with that of the corresponding bulk metal oxides. This, along with the lack of observed reaction with the limited high temperature annealing dynamics, indicates the absence of a strong driving force to form a dopant-oxide reaction product with these early transition metal dopants.

We also observe that all dopants except Ni permit bonding between the Ni(111) substrate and the terminating interfacial Al ion from the alumina coating. Even more intriguing, in all of these cases, the resulting Ni-Al bond length is nearly identical to that obtained at the clean Al<sub>2</sub>O<sub>3</sub>/Ni interface (2.25 Å), suggesting considerable reorganization of the interface to maintain Ni-Al bonds in the presence of the dopant atoms. In the case of the Ni "dopant", i.e., a rough nickel surface, the presence of the dopant inhibits Ni-Al bonding with the close-packed (111) surface. Nevertheless, the "dopant" Ni-Al bonds formed are similar in length to a higher energy clean Al<sub>2</sub>O<sub>3</sub>/Ni interfacial structure in which Ni<sub>3</sub>Al rather than NiAl bonding occurs.<sup>22</sup>

LDOS analysis can provide a detailed picture of the electronic states around each atom. As alluded to in the Theoretical Methods section, the "quantitative" measure of this analysis is somewhat limited by the fact that a projection radius over which the atom-centered s-, p-, and d-projected DOS are evaluated must be chosen. Although the choice of radius is not entirely arbitrary, it is generally necessary to find an acceptable balance between two extreme situations. A very conservative choice (small projection sphere) avoids contamination by states that should be associated with the neighboring atoms but has the unfavorable effect of leaving much of the interstitial electron density unaccounted for within the sum of LDOS projections. The alternative extreme choice, where one attempts to associate all of the electron density with atomic sites, leads to effective double counting of states between neighboring atoms, especially

**TABLE 2: Change in the Site-Projected Charges in the Interface Structure Relative to the Isolated Slab Indicated<sup>a</sup>**

interface site	interface dopant "X"						
	Ni (1.23)	Al (1.1)	Si (1.1)	Sc (1.5)	Y (1.5)	Ti (1.5)	Zr (1.5)
O relative to Al <sub>2</sub> O <sub>3</sub>	0.16, 0.16, 0.04	0.55, 0.55, 0.08	0.65, 0.65, 0.01	0.14, 0.15, 0.15	0.13, 0.14, 0.15	0.43, 0.27, 0.44	0.16, 0.16, 0.16
O relative to X-Al <sub>2</sub> O <sub>3</sub>	0.02, 0.02, -0.01	0.00, 0.00, -0.01	0.00, 0.00, 0.00	0.01, 0.02, 0.02	0.01, 0.01, 0.01	0.01, 0.04, 0.01	0.01, 0.01, 0.01
"X" relative to Ni-X	0.10, 0.11	0.18, 0.17	0.17, 0.17	0.07, 0.05	0.01, 0.02	0.37, 0.41	0.07, 0.06
"X" relative to X-Al <sub>2</sub> O <sub>3</sub>	0.12, 0.13	0.10, 0.10	0.09, 0.11	0.21, 0.20	0.08, 0.07	0.26, 0.24	0.12, 0.13
Ni relative to Ni(111)	0.04, 0.09, 0.04, 0.08	0.16, 0.21, 0.17, 0.21	0.18, 0.26, 0.20, 0.24	0.14, 0.13, 0.16, 0.14	0.12, 0.12, 0.22, 0.12	0.16, 0.16, 0.14, 0.16	0.15, 0.15, 0.15, 0.15
Ni relative to Ni-X	0.01, 0.01, 0.01, 0.00	0.15, 0.04, 0.01, 0.04	0.11, 0.07, 0.01, 0.06	0.00, 0.00, 0.11, 0.00	0.01, 0.00, 0.10, 0.01	0.14, 0.09, 0.02, 0.05	0.12, 0.03, 0.03, 0.03
Al relative to Al <sub>2</sub> O <sub>3</sub>	0.03	0.11	0.11	0.11	0.11	0.14	0.11
Al relative to X-Al <sub>2</sub> O <sub>3</sub>	-0.01	0.06	0.06	0.04	0.04	0.03	0.04

<sup>a</sup> Positive values indicate a local increase in electronic charge around the atom in the interface structure compared to the isolated slab. The projection radius (Å) for each dopant is shown in parentheses.

when metallic states are present. Whereas a judicious compromise between these two extremes might be fairly obvious in a perfect crystalline bulk structure, the optimum choice in a complicated interfacial environment is less apparent. Nevertheless, the general features from a LDOS analysis can lend valuable insight into trends and local modifications of electronic structure in diverse environments. A careful comparison of integrated LDOS values between such environments can also provide some measure of quantitative analysis, especially if such features as local bond lengths, density localization, etc. are taken into consideration.

A sense of how the site-projected charge (the integrated LDOS) is modified as a result of interface formation is logically the next required piece of information, in addition to bond lengths, for a classification of bonding interactions. Differences between the atom-centered projections of the charge in the isolated slabs and in the combined interface structure are shown in Table 2. Here, all numbers are defined explicitly in terms of the difference between the site-specific occupations in the interface environment compared to the isolated coating or substrate environment with identical ionic coordinates to the interface (where the other side of the interface has been removed "instantaneously"). The most general feature worthy of note is that, with only two minor exceptions, the interface environment results in an electronic charge increase on all of the atomic sites relative to the surfaces of the isolated pure coating and pure substrate, as well as relative to the doped coating and doped substrate surfaces. This might be expected for a "nonreactive" interface where ionic effects are limited. The electron density decay from an insulating surface follows an exponential form but is less localized for metals.<sup>61–63</sup> Hence, it is not surprising that the electron density is more localized in the interface environment, resulting in a larger effective occupancy for all site-projected charges where ionic effects are small. Furthermore, the overlap of projection spheres in all dopant-O bonds leads to a small double counting of the charge increases.

It appears from the first row of Table 2 that some of the interfacial oxygen ions are reduced quite dramatically by the presence of Al, Si, and Ti dopants (gaining 0.55 e, 0.65 e, and ~0.4 e, respectively) and are only slightly reduced (gaining ~0.15 e) by the other dopants, relative to the clean Al<sub>2</sub>O<sub>3</sub> surface. The fact that the interfacial Ti experiences a reduction (gaining ~0.4 e) similar to the oxygen implies that the increased occupation on the Ti and O atoms is due to increased localization of electron density in the form of covalent bonding. It is likely that this covalent bonding between Ti and O is largely responsible for the dramatic increase in adhesion predicted for Ti-doped Al<sub>2</sub>O<sub>3</sub>/Ni interfaces. Although the Si and Al dopants

do show some gain (~0.17 e) upon addition of the alumina coating, the corresponding much greater gain of the interfacial oxygen interacting with the dopants at those interfaces suggests that ionic or highly polar covalent effects are more pronounced in those instances. Unlike the clean Al<sub>2</sub>O<sub>3</sub> surface oxygen ions of row 1, the oxygen ions at the doped surface (row 2) are almost identical in total occupation (within ~0.01 e in most cases) to those in the interfacial environment, i.e., with the Ni(111) substrate present. Accordingly, the oxygen bonding to the dopant atom is not significantly affected by the presence of the Ni(111) slab.

The local charge analysis on the dopant metal atoms at the interface shows they have been reduced relative to the isolated surfaces (Table 2). This reduction is not achieved via explicit "charge transfer" from the oxide ions or nickel substrate, since the corresponding Ni and O generally display similar or greater gains. For instance, the interfacial Sc "dopant" experiences an increase < 0.1 e with the addition of the alumina coating (row 3), while the O ions experience a greater increase of 0.15 e (row 1); the Sc dopants experience an increase of 0.2 e in the presence of Ni(111) (row 4), while the Ni(111) surface atoms experience a corresponding increase of ~0.15 e (row 5). Instead of "charge transfer", the effective reduction primarily results from the more complete coordination, and therefore more localized electron density, around the dopant atoms in the interface environment. Table 2 shows that the dopant's effective occupation increases as a result of the coordination both with the nickel slab (interface X relative to X-Al<sub>2</sub>O<sub>3</sub>, row 4) and with the oxide (interface X relative to Ni-X, row 3). This is most dramatic in the case of Ti (~0.4 e for oxide coordination and ~0.25 e for Ni coordination), which is also calculated to be the most effective of the examined dopants in increasing adhesion at the Al<sub>2</sub>O<sub>3</sub>/Ni interface.<sup>17,18</sup>

The nickel occupancy increase at the interface follows an interesting trend (see Table 2, rows 5 and 6). Relative to the close-packed Ni(111) surface, the interfacial Ni ions experience a similar, fairly large increase in electronic charge in the presence of Al and Si dopants (0.16–0.26 e), a generally smaller increase in the presence of all early transition metal dopants (0.12–0.22 e), and a very minor increase in the case of Ni "dopant" (0.04–0.09 e). Some degree of local metallic-covalent bonding between the Ni(111) and the dopant ions occurs (see also Figure 4). Perhaps more interestingly, in comparison with the doped Ni surface, while three of the unique Ni substrate atoms at the interface experience little change in electron density (row 6), the other surface Ni atom experiences a relatively large (0.1–0.2 e) increase for all doped interfaces except Ni "dopant", where the Ni surface atoms experience no change (<0.01 e).

This charge gain on a single unique Ni interface atom is due to the Ni–Al bonding between the Ni(111)–Al<sub>2</sub>O<sub>3</sub>(0001), as shown in Table 1 (where a Ni (111)–Al bond of 2.2–2.3 Å is created for each of the interfacial dopants except Ni). In the case of Ni “dopant”, this Ni–Al bonding permits little Ni–Al interaction with the close-packed Ni(111) surface but does permit Ni–Al interactions with the undercoordinated Ni “dopants,” as also evident from Table 1 (where  $\sim 2.5$  Å Ni–Al distances correspond to Ni<sub>3</sub>Al bonding from Al<sub>2</sub>O<sub>3</sub>(0001)/Ni(111)<sup>22</sup>).

Evidence for Ni–Al bonding is supported by the fact that the interfacial Al experiences a small electronic charge increase ( $\sim 0.04$ – $0.06$  e) in the presence of the Ni(111) substrate (see also Figure 3). Furthermore, some degree of dopant–Al bonding may occur. This is apparent from the greater charge increase on the interfacial Al with the presence of Ni–X ( $\sim 0.11$  e, row 7) relative to the increase achieved with the presence of Ni(111), relative to Al<sub>2</sub>O<sub>3</sub>–X, of only  $\sim 0.04$ – $0.06$  e (row 8), i.e., some of the charge increase in the former case is due to the dopants (see also Figure 2 discussion).

From Table 2, it appears that explicit “charge transfer” across the interface is quite limited or nonexistent, insofar as no atoms experience a loss of electron density in the interface environment, i.e., all species experience either no change or electron gain. If we had considered a nonstoichiometric ceramic overlayer, it is likely that ionic effects, i.e., true charge transfer across the interface, could have played a larger role in interface stabilization. As it is, the highly anionic oxygen ions in the Al<sub>2</sub>O<sub>3</sub> coating have little driving force to oxidize additional species at the interface.

A shift in the core state eigenvalues on the interfacial atoms might provide an additional means of classifying ionic effects at the interface. This cannot be analyzed for all dopant elements in this study since the core states are not explicitly included in the self-consistent calculation of the electron density. The semi-core states of the early transition metals (i.e., 3p for Sc and Ti and 4p for Y and Zr) were included, however, and the relative eigenvalues for these states in the isolated and combined systems can be compared. These early transition metal elements initially might have appeared the most obvious choice for possible oxidation, with electronegativity values less than Ni, Al, and Si. However, no shift (within  $\sim \pm 0.1$  eV) is observed in the lowest eigenvalue for the respective 3p and 4p states between the value in the isolated dopant–Ni(111) and the interface environments. This, and the lack of charge transfer from the site-projected density analysis, suggest that true ionic bonding across the interface is quite limited.

Si and Al dopants do not result in strong (calculated) interface adhesion.<sup>17,18</sup> These dopants also have very different occupied states than the transition metals, with the Si and Al composed of mostly s and p, whereas d states comprise the major component of the early transition metals and Ni valence bands. Accordingly, we focus the remaining discussion on a comparison of the transition metal dopants at the Al<sub>2</sub>O<sub>3</sub>/Ni interface, to understand the origin of their enhanced adhesion.

Density difference plots provide a more global picture of the density modifications than can be obtained through site-projected electronic occupations. Figure 2 shows 2D slices (near the dopant–O bonds for the transition metal dopants) of the electron density differences between the interface density and the sum of the isolated Ni(111)–X and Al<sub>2</sub>O<sub>3</sub> densities. The first panel, Figure 2a, displays the Ni–O slice for the clean interface, i.e., no dopant ions present at Al<sub>2</sub>O<sub>3</sub>/Ni. Figure 2b–f shows the density difference slices for Ni, Sc, Ti, Y, and Zr dopants,

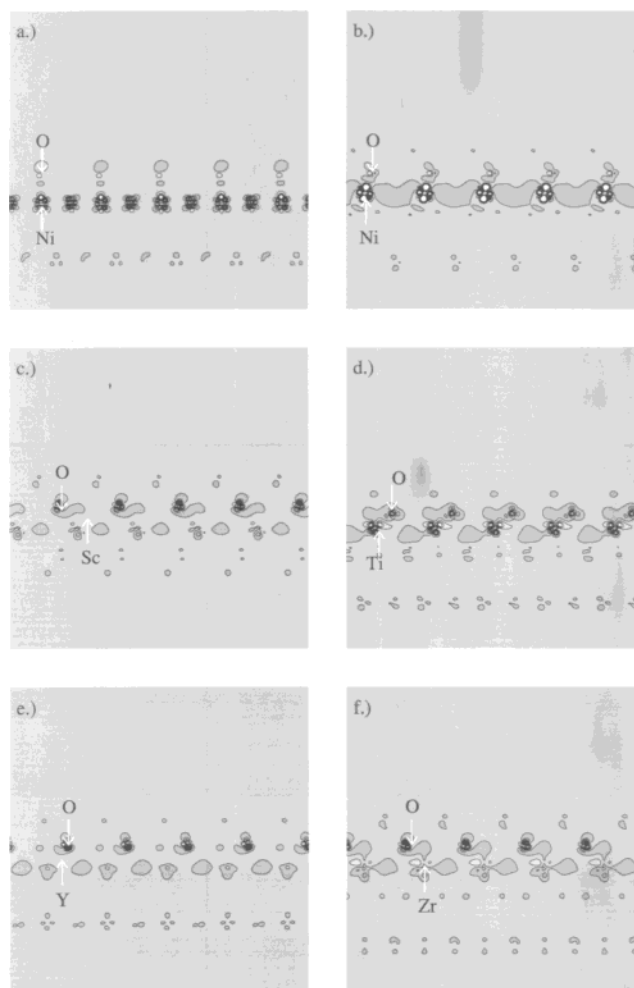


**Figure 2.** Cross-sections of the electron density differences between the interface and the sum of the isolated surface densities at a plane near the dopant–O interfacial bond. In these plots, lighter regions represent electron density loss in the interface environment relative to the isolated surfaces; and the darker regions correspond to electron density gain. All panels display the same gray scale. The background gray shade represents no significant difference in the electron density between the isolated and combined systems. Figure 2a displays the cross-section for the undoped Al<sub>2</sub>O<sub>3</sub>/Ni interface. Figure 2b–f shows the corresponding cross-sections for the interface doped with Ni, Sc, Ti, Y, and Zr, respectively. Representative ionic positions are indicated in each of the plots.

respectively. All panels display the same gray scale, with the lighter shades representing electron loss in the interface environment relative to the two free surfaces, and the darker shades representing electron density gain (each contour representing  $0.06 \text{ e}/\text{\AA}^3$ ) with interface formation. All panels in this and subsequent plots display the same gray scale. The background gray shade represents no change (i.e., roughly constant to  $\leq 0.001 \text{ e}/\text{\AA}^3$ ) between the density in the combined system and the sum of the isolated surfaces. The total charge density difference is conserved, i.e., equal to zero, within  $< 1 \times 10^{-6} \text{ e}/\text{\AA}^3$ . Although Figure 2c–f may appear to experience only charge gain, recall that these panels display only a specific perpendicular 2D cut near an interfacial bonding region. For regions that do not intersect bonds formed across the interface, there is an overall slight decrease in the delocalized density spilling into the vacuum region relative to the two surfaces.

Figure 2a,b, displaying a cross-section of Ni–O bonding, exhibits markedly different character from the plots of the early transition metal bonding with oxygen (Figure 2c–f). Both cases



with Ni–O show electron loss from the d orbital in close proximity to the oxygen. The oxygen does not show a comparable increase, although it does show a slightly increased density/localization. Ni “dopant” also experiences increased occupation in other states. This increase in the occupation of other Ni states apparent in Figure 2b and the lack of dramatic charge increase on the interfacial O ions suggest that limited ionic bonding and repulsive, nearly closed-shell (also discussed later in Figure 5) interactions may be responsible for the observed decrease in electron density in that orbital. The electron density increase in the Ni-dopant (horizontal) region is associated with Ni–Ni and Ni–Al bonding.

Figure 2c–f displays the electron density differences for Sc, Ti, Y, and Zr doped interfaces, respectively. The early transition metal doped interfaces do not exhibit behavior similar to the undoped or Ni-“doped” density difference plots. In fact, a relatively delocalized increase in electron density on the oxygen and between the dopant and the oxygen appears. This density increase between the dopant–O nuclei suggests some degree of localized, polar, covalent-type bonding between these species. This effect is most evident for Ti and Zr, which again correlates with their ability to significantly strengthen the calculated adhesion for  $\text{ZrO}_2/\text{Ni}$  and  $\text{Al}_2\text{O}_3/\text{Ni}$  interfaces.<sup>17</sup> Minor increases in electron density in the (horizontal) region of the dopant ions correspond to dopant-dopant and dopant-Al bonding, which again is most apparent for Ti and Zr dopants.

Although the metal–oxo bonding interaction is not very dramatic in these density difference plots for the early transition metal doped interfaces, there is a slight increase of electron density between the oxygen and dopants at the interface and a lack of the apparent local repulsive effects exhibited by the Ni dopant, which attempts to deplete d-states to reduce repulsion. It is likely that the metal–oxo stabilization, in the form of localized bonding and lack of repulsions, for these early transition metal dopants, relative to Ni, plays a major role in significantly strengthening the interface upon inclusion of these dopants. Similar charge-density difference effects (i.e., depletion of the d orbital interacting with the oxygen ion for late transition metal adsorbates) have been observed in the case of Ru and Pd ML versus Nb ML adsorption on thin  $\text{Al}_2\text{O}_3$  films, although in this case it was interpreted as purely resulting from polarization of the Ru and Pd and additional ionic effects for Nb.<sup>64</sup> Primarily polarization metal–oxo interactions have also been suggested for adhesion of other late transition metals such as Pt and Cu on alumina.<sup>65,66</sup> Likewise, Schweinfest et al. have shown that, although Al adhesion on  $\text{MgAl}_2\text{O}_4$  shows local bonding beyond what can be accounted for in an image charge model, the nearly-closed-shell Ag on  $\text{MgAl}_2\text{O}_4$  displays polarization interactions.<sup>67</sup>

Figure 3 displays electron density difference slices, similar to Figure 2, near the bond formed between the interface Al ion and the Ni(111) substrate. The increased density between the Ni–Al, as a result of interface formation, is strongly apparent in all panels except Figure 3b. This is to be expected from Tables 1 and 2, since the Ni dopant did not permit close bonding between the Ni(111) substrate and Al in the alumina coating. Figure 3a, similar to Figure 2a, shows the corresponding Ni–Al electron density difference for the ideal, close-packed  $\text{Al}_2\text{O}_3(0001)/\text{Ni}(111)$  interface, i.e., no dopants present. For Figure 3c–f, it appears that the Ni–Al bonding is likely to provide a significant additional source of interface stabilization. Previously, we correlated Ni–Al bonding with the relative adhesion strength at the clean  $\text{Al}_2\text{O}_3/\text{Ni}$  interface.<sup>22</sup> It appears that Ni–Al bonding similar to that which strengthened the clean interface is also present at these doped interfaces, but that the

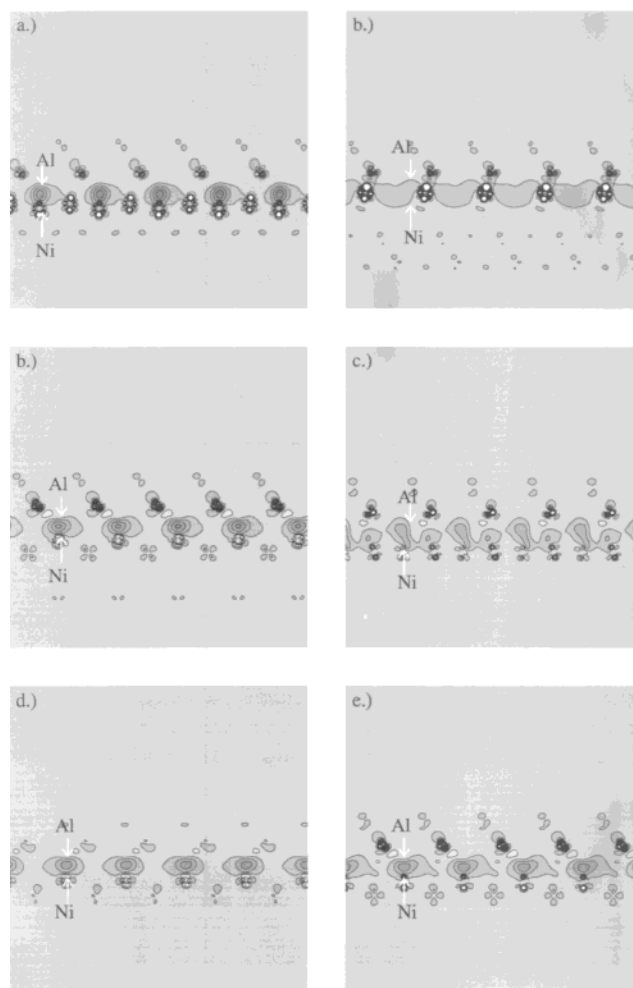


**Figure 3.** Cross-sections of the electron density difference between the interface and the sum of the isolated surface densities at a plane near the Ni substrate–Al (from the  $\text{Al}_2\text{O}_3$ ) interfacial bond. In these plots, lighter regions represent electron density loss in the interface environment relative to the isolated surfaces; and the darker regions correspond to electron density gain. All panels display the same gray scale. The background gray shade represents no significant difference in the electron density between the isolated and combined systems. Figure 3a displays the cross-section for the undoped  $\text{Al}_2\text{O}_3/\text{Ni}$  interface. Figure 3b–f shows the corresponding cross-sections for the interface doped with Ni, Sc, Ti, Y, and Zr, respectively. Representative ionic positions are indicated in each of the plots.

$\text{Al}_2\text{O}_3/\text{X-Ni}$  interface site is further stabilized by X–O interactions for the early transition metal dopants.

Figure 4 displays density difference cuts for an alternative interface cleavage site, i.e.,  $\text{Al}_2\text{O}_3\text{-X/Ni}$ , near the Ni-dopant bonds for the early transition metal dopants. All panels display an increase of electron density between the dopant–Ni(111) nuclei. The “localized” increase is most apparent for the singly coordinated Ti–Ni (Figure 4b). The localized increase in electron density between dopant–Ni nuclei is also evident for the 3-fold coordinated Ni–Sc and Ni–Zr (Figure 4a,d, respectively). The internuclear increase in Ni–Y charge density appears fairly delocalized in Figure 4c, but some increase in electron density between Ni–Y is still evident.

Dopant–Ni bonding allows these dopants to provide a strong interface, i.e., overall enhanced adhesion, rather than merely to create a new preferred site for cleavage. Weak Ni–dopant bonding interactions would permit facile cleavage between the Ni(111) and the doped alumina and limit any practical impact of doping these interfaces. As it is, the calculated cleavage

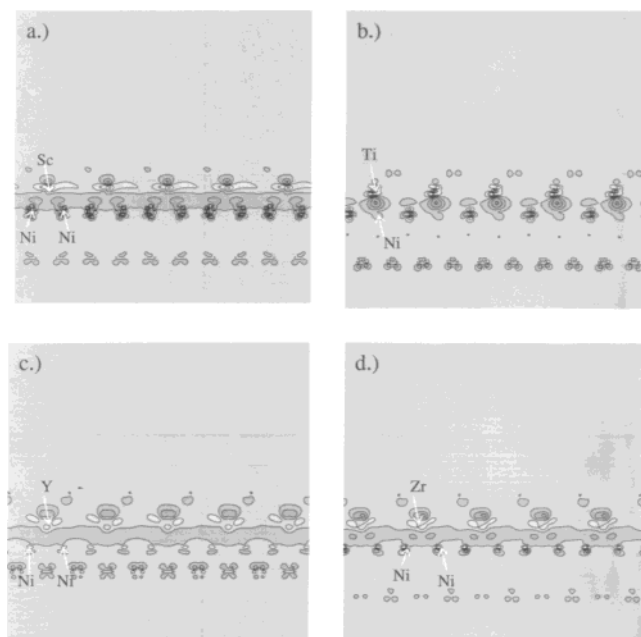


**Figure 4.** This displays a density difference cut near the dopant/Ni bond. All panels display electron density increase (darker shade of gray) between the dopant–Ni, accompanied by a slight decrease (lighter gray shade) in the horizontal dopant region. Panels a–d display the cuts for Sc, Ti, Y, and Zr-doped interfaces, respectively. All panels display the same gray scale.

energetics between the doped Ni and the alumina coating, as well as at the close-packed Ni(111) and the doped alumina interface sites, are similar ( $\sim 3\text{--}4\text{ J/m}^2$ ) to each other and to the ideal cleavage energetics for bulk Ni and  $\text{Al}_2\text{O}_3$ .<sup>18</sup> Thus, unlike the clean  $\text{Al}_2\text{O}_3/\text{Ni}$  interface, these doped interfaces are no longer the overwhelmingly preferred cleavage site. We previously indicated this could explain the observed decrease in void formation and spalling of thermal barrier coatings when early transition metals are included in the metal alloy bond coat.<sup>17</sup>

The analyses presented up to this point focus on the occupied electronic states. As mentioned earlier, donor–acceptor bond formation might have its most obvious signature in modifications of unoccupied states on the acceptor. Accordingly, Figure 5 displays the LDOS corresponding to the transition metal dopant atoms and the oxygen ion interacting with that dopant for the isolated surfaces and for the interface. The dot–dashed line indicates the Fermi level, above which all states are unoccupied at 0 K. Although this plot shows the sum of the s, p, and d LDOS projections for each ion, the features shown for the transition metals are composed almost exclusively of d states. The isolated surface states are from a self-consistent calculation of the electronic density, with ionic coordinates identical to those of the interface (with the other side of the interface removed).

Although some weak covalent bonding features might be present, the most dramatic modification for the early transition metals appears at states residing at and just above the Fermi level, i.e., the metallic/empty d states. Each of these transition metals experiences a decrease in empty d states near the Fermi level as a result of interface formation. This may reflect donor–acceptor bond formation between these dopants and the oxygen ions, i.e., the empty d states near the Fermi level acting as acceptors for  $\text{O}^{2-}$  lone pair electron density. No corresponding feature can be observed for Ni dopant; in both cases the d states are nearly fully occupied for Ni—a feature that inhibits covalent and/or donor–acceptor bonding with another closed-shell ion (i.e.,  $\text{O}^{2-}$ ). A dramatic increase in occupied states on the dopants

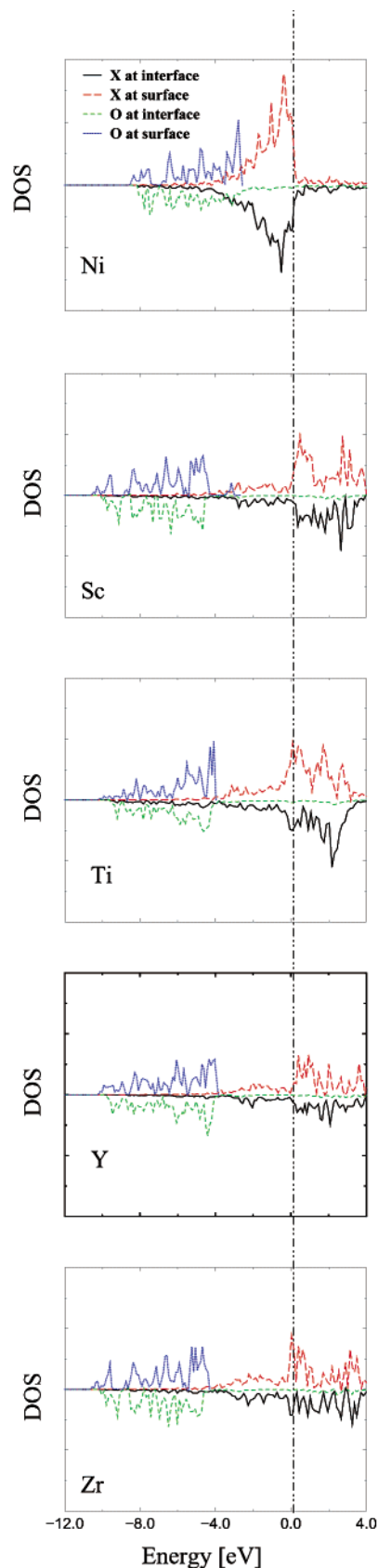


**Figure 5.** Local density of states on a transition metal dopant atom and an oxygen ion nearest to this dopant for the free surfaces (above) and the same states modified as a result of interface formation (below). The 2s states from the oxygen in the isolated surface have been aligned with the O 2s states of the interface for purposes of comparison. The dot–dashed line represents the Fermi level below which states are occupied and above which states are unoccupied at 0 K.



is not apparent, suggesting that the bonding electron density is somewhat diffuse and associated primarily with the oxygen, as also suggested by the density difference plots in Figure 2. This is to be expected in donor–acceptor bonding where the electrons originate with the donor (in this case, oxygen) and are simply partially delocalized onto the acceptor atoms.

## Conclusions

In this work, we explored how local bonding interactions can help us understand trends in adhesion at a nonreactive metal–ceramic couple,  $\text{Al}_2\text{O}_3/\text{Ni}$ , as a function of dopant. In particular, we find that local metal–metal and dopant metal–oxo interactions appear to play significant roles in determining the global adhesion strength. When both metal–metal and dopant metal–oxo interactions provide sources of attraction, the interface adhesion can be dramatically enhanced, even in the absence of a “reaction layer”.

Metal–metal bonding attractions of every type contribute to the strong interface adhesion observed with the early transition metal dopants. The density difference plots in Figure 3 indicate that Ni–Al bonding across the metal/ceramic interface, similar to that which occurs at the clean interface, also enhances adhesion at the  $\text{Al}_2\text{O}_3/\text{Ni}$  interface doped with early transition metals, despite the presence of the intermediate dopant layer. Likewise, minor increases in both Al charge (Table 2) and electron density between the dopant–Al (Figure 2) appear with interface formation. This suggests that dopant–Al interactions also serve to strengthen the  $\text{Al}_2\text{O}_3/\text{X-Ni}$  interface. Additionally, dopant–Ni bonding (Figure 4) inhibits preferential cleavage at the  $\text{Al}_2\text{O}_3/\text{X-Ni}$  interface site.

We suggest that closed-shell repulsions, which characterize the Ni–O interactions at the  $\text{Al}_2\text{O}_3/\text{Ni}(111)$  interface as well as the rough  $\text{Al}_2\text{O}_3/\text{Ni}$  interface, permit only weak adhesion at those interfaces. The metal–oxo interactions appear very different for the open-shell early transition metals compared to nearly closed-shell Ni. Decreases in the densities of low-lying empty d states on the early transition metals accompanied by a slight increase in electron density between the dopant–oxygen nuclei suggests that donor–acceptor bonding dominates, perhaps concurrent with a limited polar covalent contribution. These stabilizing metal–oxo interactions, along with an absence of closed-shell repulsions that occur for the undoped interface, correlate with the predicted increases in interface adhesion when these dopants are present, with Ti showing the most dramatic effects. It is likely this is a crucial aspect of the enhanced stabilization of these doped interfaces relative to close-packed or rough Ni surfaces.

Global interface stabilization may arise from a variety of contributions. An unbiased prediction requires a highly flexible treatment of the inter- and intra-atomic effects; it is impossible for simple models to capture a complete picture of interface interactions. As we have seen, local bonding effects may be subtle and cannot be properly included without a self-consistent treatment of the valence electron density. Such features could prove crucial to the materials properties of interest, in this case dramatically increasing the calculated “global” adhesion at an ideal interface of technological relevance.

Some ambiguity in a quantitative description of interfacial bonding remains. This is inherent to the single-determinant nature of the DFT “wavefunction”; a unique set of localized orbitals, with which to further quantify bonding interactions, does not exist. Advances in theoretical and experimental techniques, as well as in physical understanding, someday may provide a complete picture that seamlessly bridges the

microscopic to macroscopic detailed view of the behavior of heterogeneous interfaces. An increased awareness of how local bonding effects influence interface structure and strength is an important step in eventually allowing detailed, accurate predictions for improving materials used in a variety of practical applications.

**Acknowledgment.** We are grateful to the Air Force Office of Scientific Research for funding of personnel and sponsoring this research as a Challenge Project computing grant at the Maui High Performance Computing Center.

## References and Notes

- (1) Tully, J. C. *Surf. Sci.* **1994**, 299–300, 667.
- (2) Tully, J. C. *Annu. Rev. Phys. Chem.* **2000**, 51, 153.
- (3) Kindt, J. T.; Tully, J. C.; Head-Gordon, M.; Gomez, M. A. *J. Chem. Phys.* **1998**, 109, 3629.
- (4) Kindt, J. T.; Tully, J. C. *Surf. Sci.* **2001**, 477, 149.
- (5) Govind, N.; Wang, Y. A.; Da Silva, A. J. R.; Carter, E. A. *Chem. Phys. Lett.* **1998**, 295, 129. Govind, N.; Wang, Y. A.; Carter, E. A. *J. Chem. Phys.* **1999**, 110, 7677. Klüner, T.; Govind, N.; Wang, Y. A.; Carter, E. A. *Phys. Rev. Lett.* **2001**, 86, 5954. Klüner, T.; Govind, N.; Wang, Y. A.; Carter, E. A. *J. Chem. Phys.* **2002**, 116, 42.
- (6) Finnis, M. W. *Acta Metall. Mater.* **1992**, 40, S25. Finnis, M. W. *J. Phys.: Condens. Matter* **1996**, 8, 5811.
- (7) Ernst, F. *Mater. Sci. Eng. R* **1995**, 14, 97.
- (8) Christensen, A.; Jarvis, E. A.; Carter, E. A.; Atomic-Level Properties of Thermal Barrier Coatings: Characterization of Metal–Ceramic Interfaces, in *Chemical Dynamics in Extreme Environments*; Dressler, R. A., Ed.; Advanced Series in Physical Chemistry V.11; World Scientific: Singapore, 2001; p 490.
- (9) Starrost, F.; Carter, E. A. *Surf. Sci.* **2002**, 500, 323.
- (10) Broughton, J. Q.; Abraham, F. F.; Berstein, N.; Kaxiras, E. *Phys. Rev. B* **1999**, 60, 2391.
- (11) Ortiz, M.; Cuitiño, A. M.; Knap, J.; Koslowski, M. *MRS Bull.* **2001**, 26, 1.
- (12) Wang, Y. A.; Carter, E. A., in *Theoretical Methods in Condensed Phase Chemistry*; Schwartz, S. D., Ed.; Progress in Theoretical Chemistry and Physics series; Kluwer: Dordrecht, 2000; pp 117–184. Watson, S. C.; Carter, E. A. *Comput. Phys. Commun.* **2000**, 128, 67.
- (13) Goedecker, S. *Rev. Mod. Phys.* **1999**, 71, 1085.
- (14) Kohn, W. *Phys. Rev. Lett.* **1996**, 69, 3547.
- (15) Ordejón, P. *Comput. Mater. Sci.* **1998**, 12, 157.
- (16) Possible exceptions for finite temperature calculations and novel methods such as Baer, R.; Head-Gordon, M. *Phys. Rev. B* **1998**, 58, 15296.
- (17) Jarvis, E. A.; Carter, E. A. *Comput. Sci. Eng.* **2002**, 4, 33.
- (18) Jarvis, E. A.; Carter, E. A., submitted to *Phys. Rev. Lett.*
- (19) Stoneham, A. M.; Tasker, P. W. *J. Phys. C* **1985**, 18, L543. Stoneham, A. M.; Tasker, P. W. *Philos. Mag. B* **1987**, 55, 237. Tasker, P. W.; Stoneham, A. M. *J. Chim. Phys.* **1987**, 84, 149.
- (20) Finnis, M. W. *Acta Metall. Mater.* **1992**, 40, S25.
- (21) Didier, F.; Jupille, J. *Surf. Sci.* **1994**, 314, 378.
- (22) Jarvis, E. A.; Christensen, A.; Carter, E. A. *Surf. Sci.* **2001**, 487, 55 (and references therein).
- (23) Yanhui, W.; Diyong, W. *Int. J. Hydrogen Energy* **2001**, 26, 795.
- (24) Zhang, Y.; Chu, W.; Cao, W.; Luo, C.; et al. *Plasma Chem. Plasma Process.* **2000**, 20, 137.
- (25) Choy, K.-L.; She, H.-K. *Mater. Sci. Eng. A* **2000**, A281, 253.
- (26) Mo, Y. H.; Kibria, A. K. M. E.; Nahm, I. *Synth. Met.* **2001**, 122, 443.
- (27) Whittle D. P.; Stringer, J. *Philos. Trans. R. Soc. London A* **1980**, 295, 309.
- (28) Gaudette, F. G.; Suresh, S.; Evans, A. G. *Metal. Mater. Trans. A* **2000**, 31A, 1977.
- (29) Shendye, S. B.; Downham, D. A. *Oxid. Met.* **1995**, 43, 435.
- (30) Pint, B. A. *Oxid. Met.* **1996**, 45, 1.
- (31) Goward, G. W. *Surf. Coat. Technol.* **1998**, 108–9, 73.
- (32) Pint, B. A.; Wright, I. G.; Lee, W. Y.; Zhang, Y.; Prüssner, K.; Alexander, K. B. *Mater. Sci. Eng.* **1998**, A245, 201.
- (33) Haynes, J. A.; Ferber, M. K.; Porter, W. D.; Rigney, E. D. *Oxid. Met.* **1999**, 52, 31.
- (34) Pérez, P.; González-Carrasco, J. L.; Adeva, P. *Oxid. Met.* **1997**, 48, 143.
- (35) Hohenberg, P.; Kohn, W. *Phys. Rev. B* **1964**, 136, 864. Kohn, W.; Sham, L. J. *Phys. Rev. A* **1965**, 140, 1133.
- (36) Kresse, G.; Hafner, J. *Phys. Rev. B* **1993**, 47, 558. Kresse, G.; Hafner, J. *Phys. Rev. B* **1994**, 49, 14251. Kresse, G.; Furthmüller, J. *Comput. Mater. Sci.* **1996**, 6, 15.

- (37) Vanderbilt, D. *Phys. Rev. B* **1990**, *41*, 7892. Kresse, G.; Hafner, J. *J. Phys.: Condens. Matter* **1994**, *6*, 8245.
- (38) Perdew, J. P. *Phys. Rev. B* **1986**, *33*, 8822; Perdew, J. P. *Phys. Rev. B* **1986**, *34*, 7406(E). Perdew, J. P. *Electronic Structure of Solids*; Ziesche, P., Eschrig H., Eds.; Akademie Verlag: Berlin, 1991; p 11.
- (39) Rappe, A. M.; Rabe, K. M.; Kaxiras, E.; Joannopoulos, J. D. *Phys. Rev. B* **1990**, *41*, 1227.
- (40) Kleinman, L.; Bylander, D. M. *Phys. Rev. Lett.* **1982**, *48*, 1425.
- (41) Perdew, J. P.; Zunger, A. *Phys. Rev. B* **1981**, *23*, 5048.
- (42) Guénard, P.; Renaud, G.; Barbier, A.; Gautier-Soyer, M. *Surf. Rev. Lett.* **1997**, *5*, 321.
- (43) Ahn, J.; Rabalais, J. W. *Surf. Sci.* **1997**, *388*, 121.
- (44) Suzuki, T.; Hishita, S.; Oyoshi, K.; Souda, R. *Surf. Sci.* **1999**, *437*, 289.
- (45) Guo, J.; Ellis, D. E.; Lam, D. J. *Phys. Rev. B* **1992**, *45*, 13647.
- (46) Nosè, S. *J. Chem. Phys.* **1984**, *81*, 511. Nosè, S. *Prog. Theor. Phys. Suppl.* **1991**, *103*, 1.
- (47) Becker, C.; et al. *J. Vac. Sci. Technol. A* **1998**, *16*, 1000.
- (48) Rosenhahn, A.; Schneider, J.; Becker, C.; Wandelt, K. *Appl. Surf. Sci.* **1999**, *142*, 169.
- (49) Jennison J. R.; Bogicevic, A. *Surf. Sci.* **2000**, *464*, 108.
- (50) Magtoto, N. P.; et al. *Surf. Sci.* **2001**, *472*, L157.
- (51) Haynes, J. A.; Rigney, E. D.; Ferber, M. K.; Porter, W. D. *Surf. Coat. Technol.* **1996**, *86–87*, 102.
- (52) Blöchl, P. E.; Jepsen, O.; Andersen, O. K. *Phys. Rev. B* **1994**, *49*, 16223.
- (53) Methfessel, M.; Paxton, A. T. *Phys. Rev. B* **1989**, *40*, 3616.
- (54) Lewis, J.; Schwarzenbach, D.; Flack, H. D. *Acta Crystallogr.* **1982**, *A38*, 733.
- (55) Xu, Y.-N.; Ching, W. Y. *Phys. Rev. B* **1991**, *43*, 4461.
- (56) Pacchioni, G.; Sousa, C.; Illas, F.; Parmigiani, F.; Bagus, P. S. *Phys. Rev. B* **1993**, *48*, 11573.
- (57) Ching W. Y.; Xu, Y.-N. *J. Am. Ceram. Soc.* **1994**, *77*, 404.
- (58) Profeta, G.; Continenza, A.; Freeman, A. J. *Phys. Rev. B* **2001**, *64*, 045303.
- (59) Becke, A. D.; Edgecombe, K. E. *J. Chem. Phys.* **1990**, *92*, 5397.
- (60) Xu, Y.-N.; Gu, Z.-Q.; Chang, W. Y. *Phys. Rev. B* **1997**, *56*, 14993.
- (61) Kohn, W. *Phys. Rev.* **1959**, *115*, 809.
- (62) Ismail-Beigi, S.; Arias, T. A. *Phys. Rev. Lett.* **1999**, *82*, 2127.
- (63) Jarvis, E. A. A.; Hayes, R. L.; Carter, E. A. *ChemPhysChem* **2001**, *2*, 55.
- (64) Bogicevic A.; Jennison, D. R. *Phys. Rev. Lett.* **1999**, *82*, 4050.
- (65) Verdozzi, C.; Jennison, D. R.; Schultz, P. A.; Sears, M. P. *Phys. Rev. Lett.* **1999**, *82*, 799.
- (66) Łodziana, Z.; Nørskov, J. K. *J. Chem. Phys.* **2001**, *115*, 11261.
- (67) Schweinfest, R.; Kostlmeier, S.; Ernst, F.; Elsasser, C.; Finnis, M. W. *Philos. Mag. A* **2001**, *81*, 927.